

Simultaneous acceleration of two kinds of ion beams in the RISP

Siwon Jang¹ · Eun-San Kim¹

Received: 9 July 2018 / Revised: 27 December 2018 / Accepted: 18 January 2019 / Published online: 15 May 2019
© China Science Publishing & Media Ltd. (Science Press), Shanghai Institute of Applied Physics, the Chinese Academy of Sciences, Chinese Nuclear Society and Springer Nature Singapore Pte Ltd. 2019

Abstract The Rare Isotope Science Project (RISP) is a research complex consisting of a heavy-ion accelerator, which contains a front-end system, a super-conducting linear accelerator, an isotope separator online (ISOL) system, and an in-flight system. The original purpose of the post-linear-accelerator (post-linac) section was to accelerate either a stable driver beam derived from an electron cyclotron resonance ion source, or an unstable rare-isotope beam from an ISOL system. The post-linac lattice has now been redesigned using a novel and improved acceleration concept that allows the simultaneous acceleration of both a stable driver beam and a radioisotope beam. To achieve this, the post-linac lattice is set for a mass-to-charge ratio (A/q) that is the average of the two beams. The performance of this simultaneous two-beam acceleration is here assessed using two ion beams: $^{58}\text{Ni}^{8+}$ and $^{132}\text{Sn}^{20+}$. A beam dynamics simulation was performed using the TRACK and TraceWin codes. The resultant beam dynamics for the new RISP post-linac lattice design are examined. We also estimate the effects of machine errors and their correction on the post-linac lattice.

Keywords Linear accelerator · Simultaneous two-beam acceleration · Heavy-ion accelerator · Beam dynamics

1 Introduction

The Rare-Isotope Accelerator of Newness (RAON) is a key research facility of the Rare Isotope Science Project (RISP) that allows highly innovative investigations into numerous facets of basic science, such as nuclear physics, astrophysics, atomic physics, the life sciences, medicine, and materials science [1]. The RAON post-linear-accelerator (post-linac) section consists of an electron cyclotron resonance (ECR) source, an isotope separator online (ISOL) system, a low-energy-beam transport (LEBT) system, a radio-frequency quadrupole (RFQ), a medium-energy-beam transport (MEBT) system, and three superconducting linear accelerators (SCL3) [2].

The post-linac section accommodates two ion sources: a stable ion beam issued from an ECR ion source and an unstable ion beam from an ISOL system. These two ion sources share the same LEBT section up to the point where they enter the RFQ. The 81.25 MHz RFQ then accelerates the ion beams to 0.4 MeV/u. After the RFQ, a short MEBT line transports the accelerated ion beams and the matching section fits the initial beam parameters at the SCL3 entrance (Fig. 1). The post-linac section can accelerate two ion beams ($^{132}\text{Sn}^{20+}$ and $^{58}\text{Ni}^{8+}$) to 17.67 MeV/u simultaneously [3]. Different stable and radioactive beams can thus be accommodated simultaneously if they differ in their charge-to-mass ratios by up to 10%. By operating simultaneously on both beams, the post-linac section delivers two ion beams to the low- and high-energy experimental areas without retuning. The post-linac optics is primarily designed to stabilize the two ion beams during their simultaneous acceleration. This is because of the large transverse emittance of the unstable ion beams produced by

✉ Eun-San Kim
eskim1@korea.ac.kr

¹ Department of Accelerator Science, Korea University Sejong Campus, Sejong 30019, South Korea

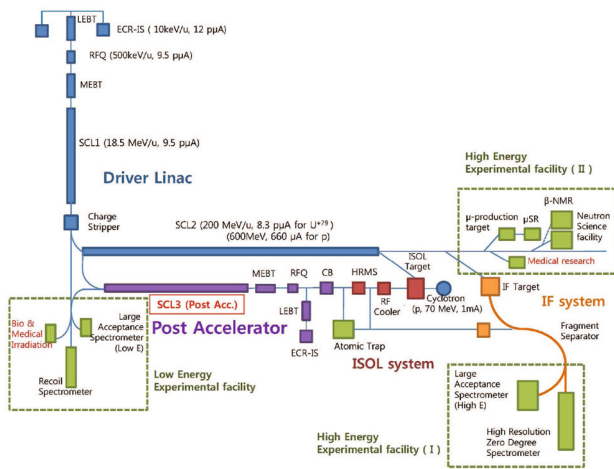


Fig. 1 (Color online) Schematic of the RISP RAON setup

the ISOL system, which has a root-mean-square (RMS) value of approximately 0.3 mm mrad.

2 Post-accelerator in RISP

The characteristics of the redesigned post-linac section are listed in Table 1. The most important lattice parameter for achieving the required two-beam acceleration is the average mass-to-charge ratio A/q for the two beams. An average A/q value of 6.925 was used to synchronize the phases at both ion-beam centers in the longitudinal direction, without incurring particle loss, as shown in Fig. 2.

The post-linac lattice employs two types of cavity, encompassing energies ranging from 0.4 to 17.67 MeV/u. Quarter-wave resonator (QWR) and half-wave resonator (HWR) cavities are used, respectively, in the low- and medium-energy acceleration regimes, up to 17.67 MeV/u. The QWR cavities are operated at 81.25 MHz, which equals the ion-beam bunch repetition rate (i.e., at 0.047 of

Table 1 Basic parameters in the post-linac section

Parameters	Value
Stable particle type (A/q)	$^{58}\text{Ni}^{8+}$ (7.25)
Unstable particle type (A/q)	$^{132}\text{Sn}^{20+}$ (6.6)
Average A/q	6.925
Repetition rate (MHz)	81.25
Beam energy (MeV/u)	0.4–17.67
Number of QWR cavities	21
Number of HWR cavities	98
Number of quadrupole magnets	104
Linac length (m)	98.21

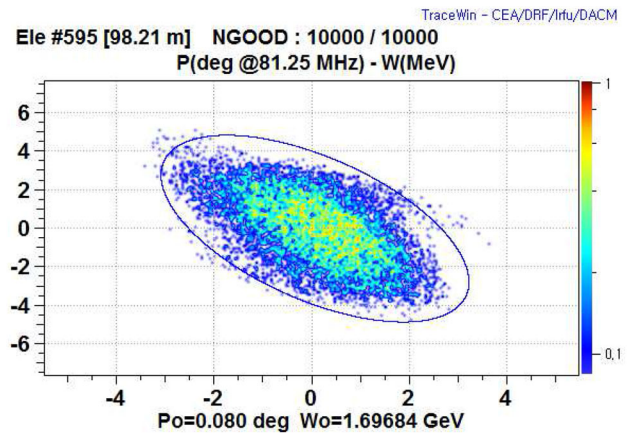


Fig. 2 (Color online) Longitudinal beam distribution of the average A/q value beam at the end of SCL3

the geometric β), while the HWR cavities are operated at 162.5 MHz (0.12 of the geometric β). The peak electric-field strength in both the QWR and HWR cavities in the lattice design is 35 MV/m [4].

The energy gains of the two cavity types and their effective energy ranges are shown in Fig. 3. The energy transition value between the QWR and HWR sections is 2.59 MeV/u ($\beta \sim 0.074$), which was chosen to increase the acceleration efficiency in the HWR section. The lattice-structure parameters for each post-linac segment are shown in Fig. 4. A single period within the β_1 (QWR) segment consists of one QWR inside a cryomodule, a quadrupole doublet, and one beam box, with the beam box including various types of beam-diagnostic equipment. The period length of each β_1 period with a QWR cavity is 1.13 m, and there are 21 periods in the β_1 segment. The β_2 -segment (HWR1) cryomodules include two HWR cavities, while the β_3 -segment (HWR2) cryomodules include four HWR cavities. These two HWR segments are used to achieve an accurate alignment and a highly efficient ion-beam

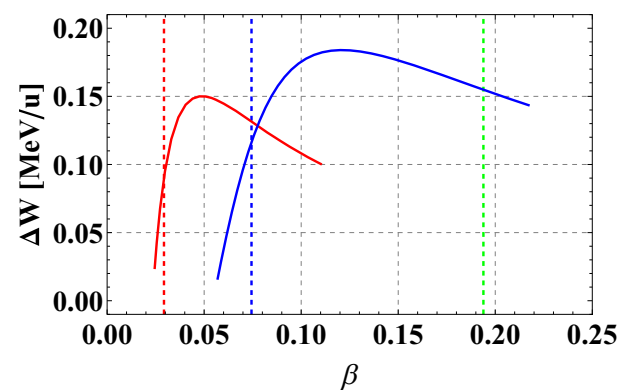


Fig. 3 (Color online) QWR and HWR cavity energy gains plotted as functions of β . The red, blue, and green dotted lines denote the initial post-linac beam energy, the QWR-to-HWR transit energy, and the final energy, respectively

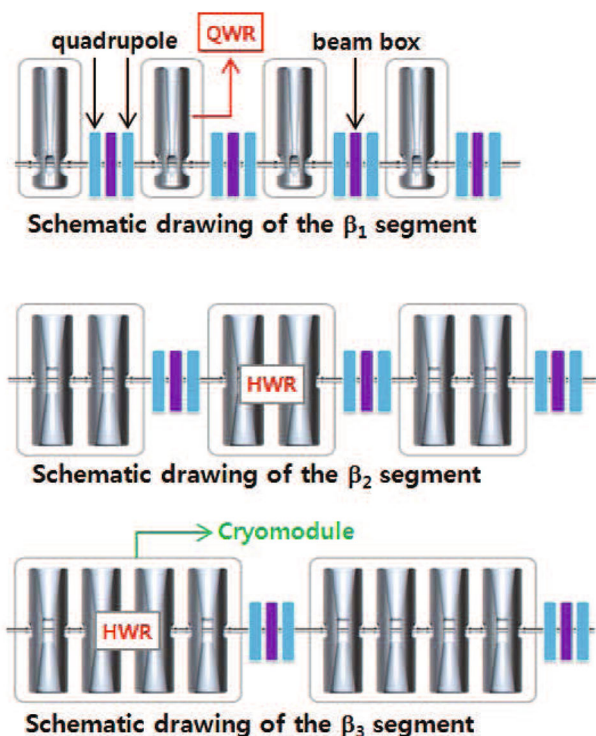


Fig. 4 (Color online) Layout of the QWR and HWR sections

acceleration. The periods of the HWR1 and HWR2 segments also include two quadrupoles and one beam box for the purposes of beam focusing and diagnostics. The period lengths of the β_2 and β_3 segments are 1.8 and 2.68 m, respectively, and the number of periods is 13 and 18, respectively. Detailed parameters for each of the β segments are listed in Table 2.

3 Evaluation of the post-linac lattice design and beam dynamics for simultaneous two-beam acceleration

To perform single-ion-beam acceleration, two different post-linac lattice designs were used to accelerate ions with different values of A/q . $A/q = 7.25$ for a stable Ni ion beam, and 6.6 for an unstable Sn radioisotope (RI) beam. As noted above, the RAON post-linac lattice was redesigned to allow simultaneous two-beam acceleration. Therefore, a lattice was established, corresponding to the average value $A/q = 6.925$ for the Ni and Sn ion beams. This average value allows the synchronization of the phases at the center of both ion beams.

To avoid increasing the beam emittance and the envelope instability, the post-linac lattice was designed with the following conditions. The phase advance of the zero-current beam in the transverse and longitudinal directions (σ_{10} and σ_{10} , respectively) must be less than 90° per focusing

Table 2 RAON post-linac β -segment parameters

Parameters	Values
QWR (β_1) segment	
Length (m)	23.73
Period length (m)	1.13
Period number	21
Cavity number	21
Cavity number per cryomodule	1
Frequency (MHz)	81.25
Geometric beta, β_g	0.047
W_{out} (MeV/u)	2.59
E_{peak} (MeV/u)	35
HWR1 (β_2) segment	
Length (m)	23.40
Period length (m)	1.8
Period number	13
Cavity number	26
Cavity number per cryomodule	2
Frequency (MHz)	162.5
Geometric beta, β_g	0.12
W_{out} (MeV/u)	5.93
E_{peak} (MeV/u)	35
HWR2 (β_3) segment	
Length (m)	50.92
Period length (m)	2.68
Period number	18
Cavity number	72
Cavity number per cryomodule	4
Frequency (MHz)	162.5
Geometric beta, β_g	0.12
W_{out} (MeV/u)	17.67
E_{peak} (MeV/u)	35

period, to prevent envelope instability at high current. However, the RAON post-linac lattice has a very low beam current for both the stable and unstable beams. The phase advance per cell in the post-linac segment is therefore initiated at 100° , as shown in Fig. 5. The wave numbers in the transverse and longitudinal directions, κ_{10} and κ_{10} , respectively, indicate the strength of the focusing force in each period and should vary smoothly along the entire linac. This lattice-conversion condition decreases the latent risk of mismatching and reduces the sensitivity of the linac to the beam current. Such requirements for lattice design are very important for the lattice transition section. In that section, the periods are broken because of the practical limit on the cryomodule length, or because of changes in the composition of the superconducting cavity. Then, κ_{10} and κ_{10} obey

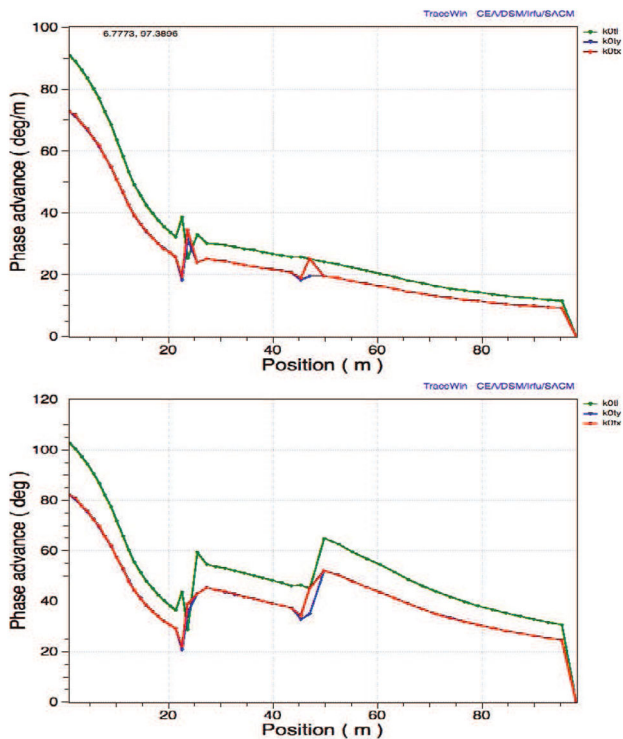


Fig. 5 (Color online) Phase advances per meter (upper figure) and per period (lower figure)

$$\sigma_{t0} = \frac{\kappa_{t0}}{L_0}, \quad \sigma_{l0} = \frac{\kappa_{l0}}{L_0}, \quad (1)$$

where L_0 denotes the length of the focusing period [5].

The exchange of energy between the transverse and longitudinal directions may result from space-charge resonance and should be avoided. The working point of each cell should therefore be positioned far from the unstable area, as shown in Fig. 6. The working points of each period are here clearly positioned to avoid the resonant area. The transition lattice-matching section achieves a precise matching between the lattices of the different cavities, thus preventing an increase in beam emittance and a discontinuity in the beam envelope. The envelope at the lattice transition section should therefore change as

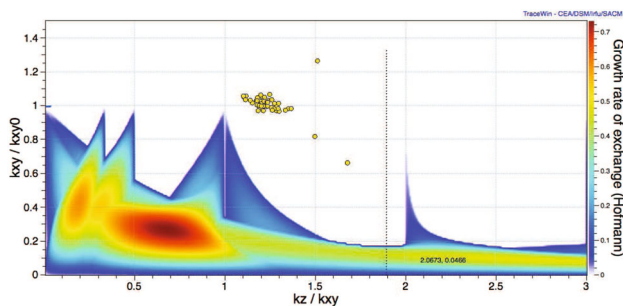


Fig. 6 (Color online) Post-linac section Hofmann chart. The working points in every period are positioned to avoid the resonant area

continuously as possible, thereby avoiding strong peaks in the envelope along the linac.

The values of σ_{t0} and σ_{l0} at zero current in each focusing period are shown in Fig. 5. Some abrupt changes are apparent in the transition section because the periodic lattice is broken by splitting the cryomodule into two parts. Three cavities and four quadrupoles were calibrated to achieve a matching between the two cryomodules, hence to prevent the formation of a strong peak in the transition section, in both the transverse and longitudinal planes. Figure 7 shows σ_{t0} and σ_{l0} in each period, where the phase-advance ratio was fixed to 0.8 to maintain the quadrupole field strength below 25 T/m. Figure 8 shows the quadrupole field strength along the post-linac section, with a maximum field strength of approximately 25 T/m. Note that the quadrupole magnets have a 50-mm aperture to allow the installation of a stripline beam-position monitor (BPM). Figure 9 shows the beam envelope of RMS and maximum of SCL3. The maximum envelope do not exceed 20mm of beam pipe radius.

Figure 10 shows the beam emittances for the simultaneous two-beam particle-tracking simulation with 20,000 particles traversing the post-linac section. The RMS transverse beam emittance is slightly increased in the vertical direction and the two beams are well focused until the end of the post-linac section. The RMS initial normalized beam emittances in the horizontal and vertical directions are 0.3118 and 0.3099 mm mrad, respectively, and the emittance growth rates in the horizontal and vertical directions are 1.8% and 29.3%, respectively. The RMS initial longitudinal beam emittance is 0.5185 keV/u · ns. The RMS normalized longitudinal emittance increases approximately threefold. This is because the longitudinal beam centers of the two ion beams at the end of the linac section are split, so that the entire longitudinal emittance is increased. RMS single-beam emittances, calculated using a tracking simulation, are shown in Fig. 11. The RMS longitudinal emittances of the $^{132}\text{Sn}^{20+}$ and $^{58}\text{Ni}^{8+}$ beams are increased by only 6.8% and 17.7%, respectively.

Figure 12 shows the effective radio-frequency (RF) voltage used (as opposed to the nominal voltage) for both types of super-conducting cavity. This is the optimized

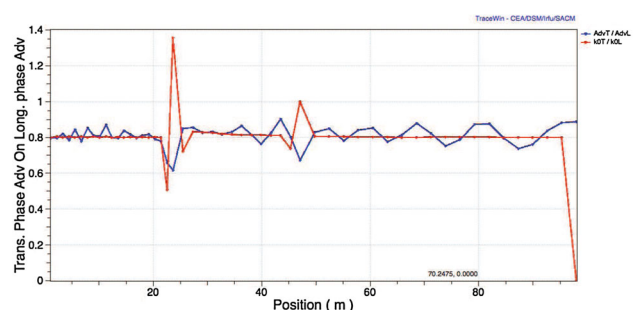


Fig. 7 Transverse and longitudinal phase advances in each period

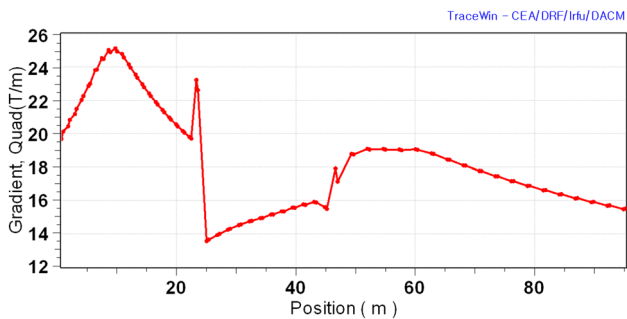


Fig. 8 Quadrupole field strength. Using a lattice design with a lower phase-advance ratio, the field strength was calibrated to lie below 30 T/m everywhere

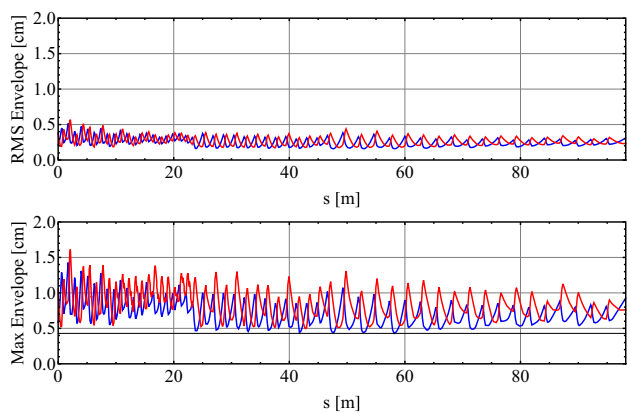


Fig. 9 Post-linac beam envelope: RMS (top) and peak values (bottom)

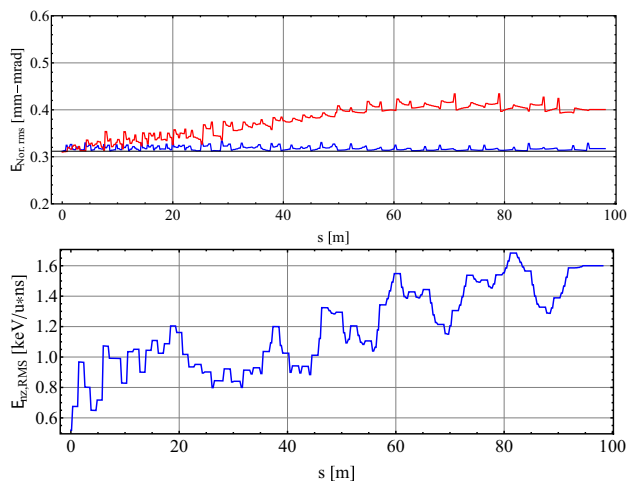


Fig. 10 Transverse (top) and longitudinal (bottom) emittances at the post-linac exit

result obtained by enforcing the requirements for the phase advance, for a smooth change in focusing, and for the longitudinal acceptance. Another limitation on the effective field level is associated with the multipacting effect in the superconducting cavities. The E peak voltage should

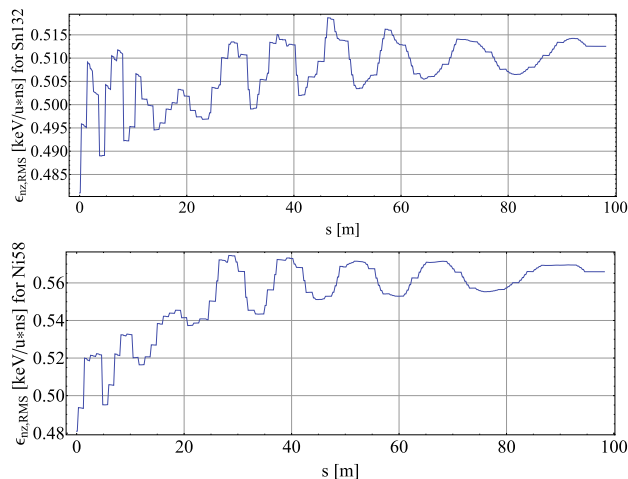


Fig. 11 RMS single-beam longitudinal emittance determined using a tracking simulation for $^{132}\text{Sn}^{20+}$ (top) and $^{58}\text{Ni}^{8+}$ (bottom)

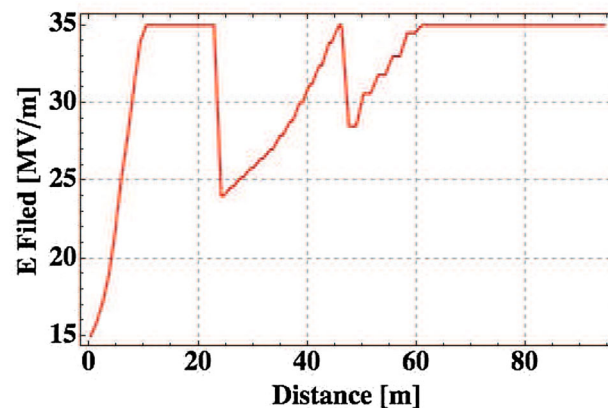


Fig. 12 Post-linac field map factor. To obtain a large RF acceptance, the initial QWR cavity fields are set to a low level, but no RF cavity multipacting effects are observed

not be lower than 15 MV/m, to avoid working within the multipacting regions. To reduce beam loss, the synchronous phase increases smoothly from -40° to -30° in

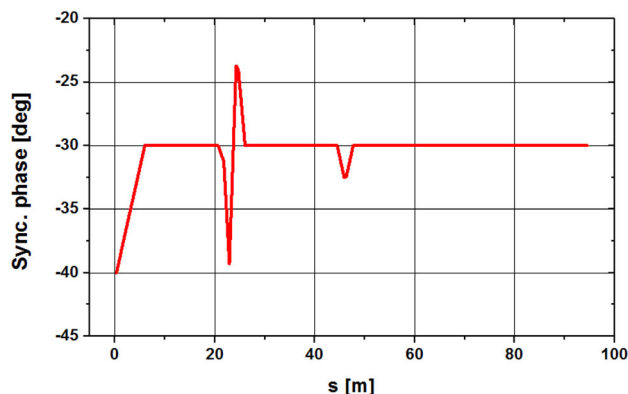


Fig. 13 Synchronous phase in the post-linac section

the QWR section, as shown in Fig. 13. The simultaneous two-beam energy variation along the post-linac section is shown in Fig. 14. The two-beam energy increases from 0.4 to 17.67 MeV/u.

Detailed multi-particle simulations were performed for the SCL3. The first step involved studying the dynamic behavior of the SCL3 beam core using an initial 6D water-bag beam distribution. Notably, the QWR cavities displayed steering effects in the transverse direction [6]. This implied a need to correct the beam orbit, despite the absence of any errors. The top figure in Fig. 15 shows the SCL3 beam envelope displaying steering effects in the QWR section, while the bottom figure shows the SCL3 beam envelope obtained after using several steering magnets to apply the beam-orbit correction.

The longitudinal acceptance of the SC section was analyzed using the TraceWin code, assuming zero current. The initial longitudinal emittance was set to a sufficiently large value. In our analysis, particles with energies and phases greater than 0.5 MeV and 120° , respectively, were defined as lost particles. These particles, which can be tracked through the lattice, were used to calculate the acceptance, plotted in Fig. 16. The RF acceptance is calculated to be $15.56 \text{ keV}/u \cdot \text{ns}$.

Figure 17 shows the results of the simultaneous two-beam multi-particle-tracking simulation at the end of the RAON post-linac section. The $^{132}\text{Sn}^{20+}$ radioactive beam from the ISOL system and the stable $^{58}\text{Ni}^{8+}$ beam, which is commonly produced at an ECR source, are shown in red and green, respectively. Note that, at the end of the post-linac section, the $^{58}\text{Ni}^{8+}$ beam is extracted to be transferred to a low-energy experimental area, while the $^{132}\text{Sn}^{20+}$ beam is injected into the SCL2 section for further acceleration.

4 Machine-error evaluation and correction

4.1 Machine-error evaluation

The main sources of error in the post-linac section are element misalignments and discrepancies in RF-system

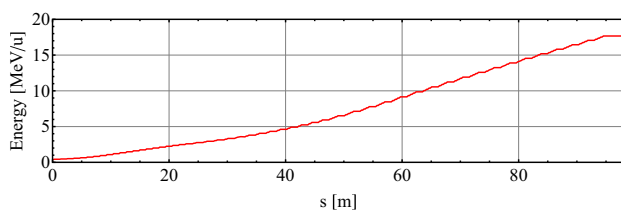


Fig. 14 Simultaneous two-beam energy variation along the post-accelerator section. The two ion beams are accelerated to 17.67 MeV/u

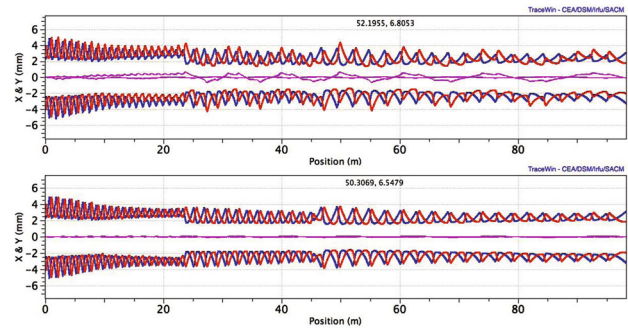


Fig. 15 Post-linac QWR steering effects: the beam orbit before (top) and after (bottom) correcting for QWR steering effects

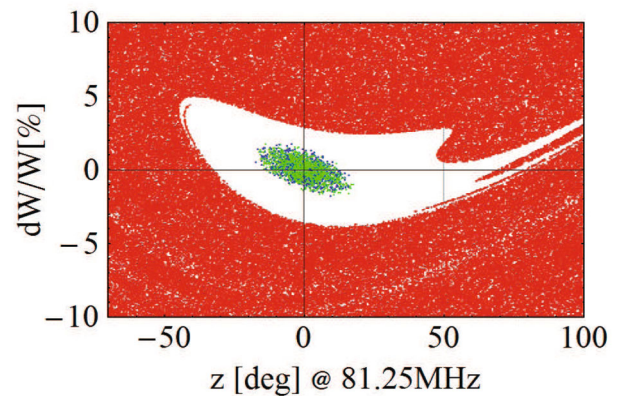


Fig. 16 (Color online) Post-linac RF acceptance

precision and stability [7–9]. Typical values for such errors are listed in Table 3. For the error simulation discussed here, all error values were randomly generated according to the specified distribution. The uniform distributions were defined as spanning the extreme values (i.e., $\pm \text{max}$), and the Gaussian distributions were truncated beyond ± 3 RMS values. Displacement errors were applied to the x and y positions of the element ends, while rotation errors were applied around the z (beam) axis. To determine the statistical significance, simulations were repeated 500 times, with each iteration beginning with a different seed from a random number generator. Two thousand particles were tracked in each simulation.

4.2 Machine-error correction

To determine the effects of these machine errors on the linac performance, we simulated the behavior with and without error correction. Transverse correctors and the errors listed in Table 3 were employed in the simulation. Figure 18 shows the resultant centroid beam orbit along the post-linac section, with the results before and after applying correction results shown in blue and red, respectively. Before applying the correction, it is clear that the centroid

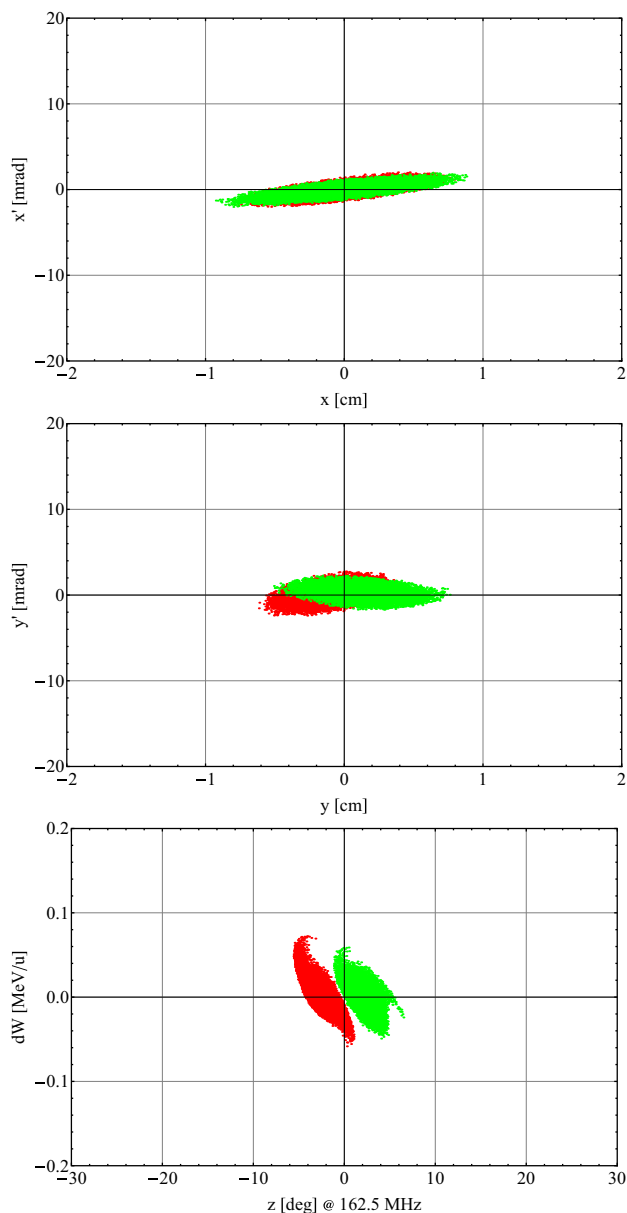


Fig. 17 (Color online) Beam distributions at the exit of the post-linac section

Table 3 Post-linac sources of error and typical values

Error	Value	Distribution
Quad displacement	0.15 mm (max)	Uniform
Quad rotation (z-axis)	5 mrad (max)	Uniform
Quad field error	1% (RMS)	Gaussian
Cavity displacement	1 mm (max)	Uniform
Cavity field error	1% (RMS)	Gaussian
Cavity phase error	1% (RMS)	Gaussian

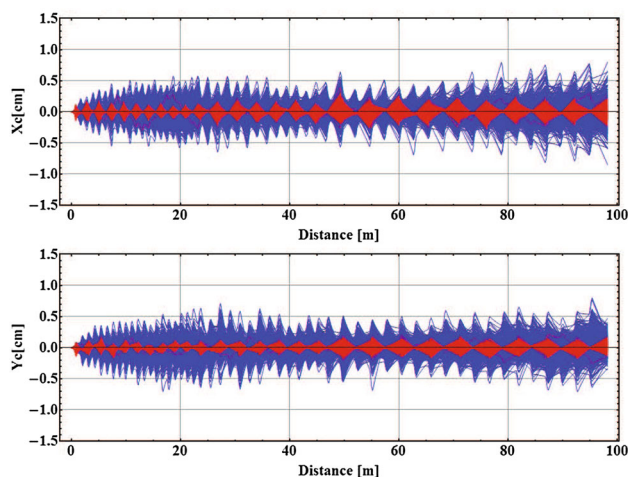


Fig. 18 (Color online) Simulated two-beam centroid beam orbit with (red) and without (blue) correction

beam orbit is significantly degraded. In particular, the RMS centroid orbit in the vertical direction deviates by 8 mm at most. After applying the transverse corrections, the centroid orbits are well corrected along the beam center. Figure 19 shows the RMS beam emittance along the post-linac section, multiplied by 4 (4×). For the orbit correction, we used two BPMs and two correctors, within two periods. The 4× RMS vertical emittance was increased approximately four times relative to the case with error. Further, the 4× RMS transverse emittance was significantly

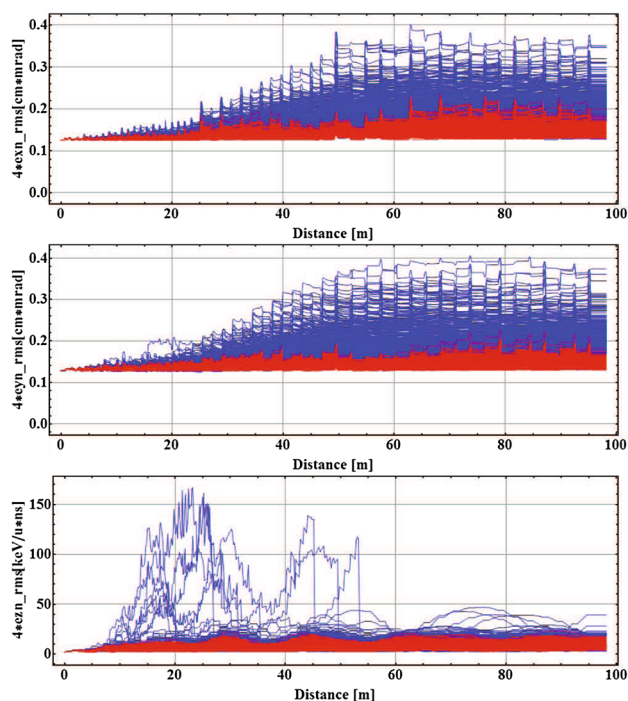


Fig. 19 (Color online) Vertical, longitudinal, and transverse two-beam simulation beam emittances with (red) and without (blue) correction

reduced after the correctors were applied. The $4\times$ RMS longitudinal emittance increased significantly for a small number of seed values, but was also significantly reduced following orbit correction.

5 Conclusion

An analysis of beam dynamics in the RAON post-linac lattice was performed under the condition of simultaneous two-beam acceleration. First, the lattice was redesigned to accommodate both a stable ion beam and an RI beam simultaneously. Further, the A/q of the post-linac lattice was adjusted to 6.925, i.e., the average A/q of the two individual ion beams. The designed post-linac section employs QWR and HWR cavities to facilitate two-beam acceleration. Each periodic lattice contains two quadrupole magnets and a single beam-diagnostics box. The phase advance per meter over the entire lattice was designed to be below 90° to prevent resonance effects. The two ion beams were accelerated from 0.4 to 17.67 MeV/ u and the RF acceptance of the post-linac section was 15.6 keV/ $u \cdot$ ns. Thanks to this redesigned post-linac lattice, the two ion beams were accelerated without beam loss. Machine error was also evaluated to establish the effects of machine imperfections on performance. Several misalignment and field-strength errors were considered. It was found that the centroid orbit was well corrected within 3 mm by applying a vertical correction scheme, and the $4\times$ RMS emittance

was also well corrected. Future work will investigate a start-to-end simulation of the simultaneous two-beam acceleration.

References

1. RISP web site. <http://risp.ibs.re.kr>
2. E.-S. Kim, J.B. Bahng, J.-G. Hwang et al., Start-to-end simulations for beam dynamics in the RISP heavy-ion accelerator. Nucl. Instrum. Methods A **794**, 215–223 (2015). <https://doi.org/10.1016/j.nima.2015.05.044>
3. B. Mustapha, P. Ostroumov, A. Perry, et al., Simultaneous acceleration of radioactive and stable beams in the ATLAS linac, TH01AB01, in *Proceedings of HN2014, East-Lansing, MI, USA*
4. D.-O. Jeon, Status of the RAON accelerator systems, in *Proceedings of IPAC2013, Shanghai, China, THPWO062*
5. P.N. Ostroumov, B. Mustapha, J.-P. Carneiro, Beam dynamics studies of the 8-GeV linac at FNAL, TH301, in *Proceedings of LINAC08, Victoria, BC, Canada*
6. P.N. Ostroumov, K.W. Shepard, Correction of beam-steering effects in low-velocity superconducting quarter-wave cavities. Phys. Rev. Spec. Top. Accel. Beams **4**, 110101 (2001).
7. P.N. Ostroumov, B. Mustapha, V.N. Aseev, Beam dynamics studies of the 8-GeV Superconducting H^- Linac, TUP072, in *Proceedings of LINAC 2006, Knoxville, TN, USA*
8. P.N. Ostroumov, V.N. Aseev, B. Mustapha, Beam loss studies in high-intensity heavy-ion linacs. Phys. Rev. Spec. Top. Accel. Beams **7**, 090101 (2004)
9. J.-P. Carneiro et al, Beam loss due to misalignments, RF jitter and mismatch in the Fermilab PROJECT-X 3 GEV CW Linac, FERMILAB-CONF-12-199-APC